ARTICLE   OPEN

Check for updates

Sea–air coupling leads to a decrease in precipitation in East Asia under present day conditions that is partially alleviated in future simulations

Jing Peng [1]✉, Kai Li[1,2]✉, Li Dan[1], Xiba Tang[3], Zhongfeng Xu[1], Liwei Zou[4], Hui Zheng[1] and Taotao Zhang[2]

The offshore region of East Asia has a crucial role in recycling precipitation, especially in the current context of a warming climate. This is because the atmospheric feedback from the sea offshore East Asia directly impacts and modifies precipitation patterns by influencing the seasonal cycles of the surface energy and water budgets. We used a regional climate model incorporating sea–air coupling to investigate and better understand these climate feedback mechanisms in East Asia. We identified a reduction in precipitation caused by sea-air coupling over East Asia during the time period 1991 − 2014 under present day conditions. Specifically, we observed an average decrease in precipitation of about 0.1 ± 0.40 mm day^{-1} during June–July–August. This decrease in precipitation can be attributed to a combination of factors, including the effects of upward solar radiation, the asymmetry of the thermal contrast between the land and the sea, decreased evaporation in the southeastern ocean and the weakened transport of water vapor from the sea to the land. Our research suggests that the decrease triggered by sea–air coupling will be partially alleviated under future conditions, although not completely reversed, in terms of its impact on precipitation in eastern China. Although some relief is anticipated, the overall influence of sea–air coupling on patterns of precipitation in East Asia will persist, especially south of the Yellow River in eastern China.

INTRODUCTION

East Asia, a densely populated region that is currently undergoing rapid economic development, is increasingly vulnerable to water resource challenges[1]. The region's susceptibility to changing precipitation patterns presents significant hurdles, including threats to food security and environmental degradation[2]. It is therefore crucial to both understand and forecast the impact of the natural climate system on East Asia's climate and hydrological cycle[3,4] and, in particular, to understand the underlying physical and dynamic mechanisms driving these changes[5]. Incorporating these mechanisms into the models used for qualitative assessments and projections across various timescales, ranging from seasonal to multi-annual, is essential for effective planning and decision-making processes[6,7].

The hydrological cycle in East Asia is influenced by two dominant monsoon systems: the East Asian summer monsoon and the East Asian winter monsoon[8,9]. The summer monsoon has a crucial role in determining the region's annual precipitation patterns[10,11]. The East Asian summer monsoon is characterized by two distinct systems of rain belts that contribute the majority of the seasonal rainfall across a wide latitudinal span. One of these rain belts stretches from East China to Japan and usually covers China, Korea and Japan. The other rain belt is located over the tropical western Pacific[8]. These rain belt systems are integral to the distribution of precipitation in East Asia and have a significant impact on the region's water resources and ecosystems[12,13].

A dominant southwesterly flow prevails during the boreal summer, carrying abundant moisture and warmth from the tropical western Pacific[14,15]. There is increasing recognition among researchers of the crucial impact of sea–air interactions on precipitation patterns in East Asia[10]. Sea–air interactions have a pivotal role in our understanding of various climate phenomena in East Asia. In the Pacific Ocean, they contribute to the El Niño–Southern Oscillation and the Pacific Decadal Oscillation, whereas in the North Atlantic they influence the North Atlantic Oscillation and the Atlantic Multidecadal Oscillation[13,16–20]. These climate patterns have significant impacts on the East Asian monsoon and the recycling of precipitation. There is a noticeable decrease in precipitation in both South and North China during the warm phase of the El Niño–Southern Oscillation and the Pacific Decadal Oscillation, whereas an increase in precipitation is observed around the Yangtze River area[21–23]. These sea–air interactions and teleconnections underscore the significant influence of the ocean in facilitating the transport of moisture and the shaping of precipitation patterns in East Asia.

The importance of ocean coupling in regional Earth system models, particularly in the context of East Asia, has gained widespread recognition[24,25]. Sensitivity analyses consistently highlight the significance of sea–air coupling in the accurate simulation of the East Asian summer monsoon in regional models[26,27]. The superiority of regional sea-coupled simulations over uncoupled simulations in capturing the climatological characteristics and the interannual variability of precipitation has been demonstrated in a number of studies[28,29].

The advantages of coupling a regional climate model with the ocean component have been emphasized[30]. This coupling

[1]CAS Key Laboratory of Regional Climate-Environment for Temperate East Asia, Institute of Atmospheric Physics, Chinese Academy of Sciences, Beijing 100029, China. [2]Key Laboratory of Meteorological Disaster (KLME), Ministry of Education & Collaborative Innovation Center on Forecast and Evaluation of Meteorological Disasters(CIC-FEMD), Nanjing University of Information Science & Technology, Nanjing, China. [3]Laboratory of Cloud-Precipitation Physics and Severe Storms (LACS), Institute of Atmospheric Physics, Beijing 100029, China. [4]State Key Laboratory of Numerical Modeling for Atmospheric Sciences and Geophysical Fluid Dynamics (LASG), Institute of Atmospheric Physics, Chinese Academy of Sciences, Beijing 100029, China. ✉email: pengjing@tea.ac.cn; likai@tea.ac.cn
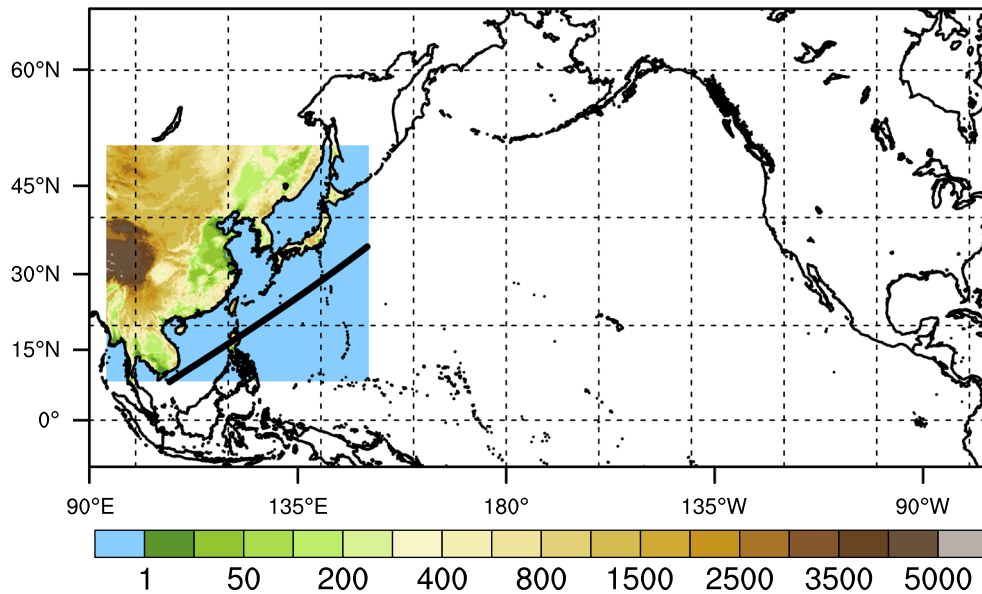
Fig. 1 The model domains and experiments design. The color filled areas represent the terrain height distribution of the whole regional air-land-sea coupling CPL domain that this study focused. The atmospheric and oceanic models completely couple in the most region of the color filled domain except a few ocean regions of west 98°E in the color filled regions. Only oceanic model is forced by the bias-corrected combined global data set outside the interactive ocean areas over the North Pacific (10°S-66.0°N, 98°E-74.9°W). The solid black slash-line on the color filled domain divides the atmosphere-ocean coupling area into offshore and distant sea regions.

approach has led to substantial improvements in the correlation between rainfall and sea surface temperatures (SSTs) in the tropical western North Pacific (WNP), particularly near the Philippines and the surrounding seas adjacent to the Korean Peninsula. These studies collectively underscore the benefits of incorporating ocean coupling in regional models. By doing so, these models can provide a more precise representation of rainfall patterns and the associated climate features in East Asia, enhancing our understanding of the region's climate dynamics.

Seasonal sea–air interactions provide valuable insights into the performance of atmospheric general circulation models driven by the observed SSTs[31]. These interactions underscore the significance of ocean coupling because simulations lacking this coupling tend to exhibit a lower performance. The lack of ocean coupling in regional climate models, which traditionally prioritise land-atmosphere interactions, has been associated with suboptimal precipitation simulations in East Asia, thereby limiting our understanding of atmosphere-ocean dynamics[4,32]. To address this limitation, we used a fully coupled regional climate model (RCM) encompassing air, land and sea components to investigate changes in precipitation. Our primary objective was to gain insights into the intricate dynamics following ocean coupling and their impact on precipitation anomalies in East Asia (Fig. 1). We analyzed both present (1991−2014) and future (2016−2039) scenarios after incorporating sea–air coupling.

RESULTS

Sea–air coupling leads to weakened precipitation and circulation over land in East Asia

We used simulations UNC and CPL to estimate the precipitation during the time period 1991–2014 under present day conditions. We specifically selected this time frame to ensure the comparability of our results with the dataset provided by the Tropical Rainfall Measuring Mission (TRMM) (Supplementary Fig. 1), TRMM Multi-satellite Precipitation Analysis daily datasets in 0.25° spatial resolution from 1998–2014. It's important to note that the correlations in Supplementary Fig. 1 are spatial correlations and cover the entire region shaded in Fig. 1, including both land and

ocean. Our investigation showed that incorporating ocean–atmosphere coupling yielded more precise precipitation during JJA estimates than the control simulation. Our analysis showed that the standardized deviations of simulation CPL under present day conditions showed lower mean values during JJA than simulation UNC. The decrease in mean values was approximately 0.02 mm day^{-1}.

In addition, supplementary Figs. 2 and S2 show the spatial distribution of original precipitation, correlations and root mean square error (RMSE) for both UNC and CPL simulations compared to observations. From the spatial distribution, the correlation of CPL with observations is equal to that of UNC with observations during summer by 0.6 (Fig. 2e, f). In addition, the simulation RMSE decreases slightly from 6.2 mm day^{-1} for simulation UNC to 6.1 mm day^{-1} for simulation CPL. In winter the correlations are quite similar and the simulation errors remain the same (Supplementary Fig. 2e–f).

Supplementary Fig. 3 shows the pattern in the precipitation anomalies after ocean coupling. The mean average annual precipitation for the whole domain was reduced by 0.008 ± 0.10 mm day^{-1} from 1991 to 2014 compared with the control experiment. The decrease in the mean JJA precipitation of East Asia of −0.13 ± 0.28 mm day^{-1} was greater than that of the ocean of −0.03 ± 0.77 mm day^{-1} (Fig. 3a). Conversely, a slight decrease in the average precipitation anomalies over land in JJA was estimated as +0.014 ± 0.25 mm day^{-1} under the future conditions from 2016 to 2039. The increase in ocean precipitation during 2016 − 2039 was even greater at 0.09 ± 0.61 mm day^{-1}.

Our study showed a distinct spatial pattern of changes in precipitation following the introduction of ocean coupling (Fig. 3 and Supplementary Table 1). We observed a reduction in both summer (JJA) and winter (DJF) precipitation over the land surfaces, with a high consistency between present and future conditions. Specifically, East China and South China experienced the steepest decrease in JJA precipitation, with a reduction of 0.19 mm day−1. However, East Asia experiences the local winter during DJF and the precipitation anomalies are obscure. From a seasonal perspective, these precipitation anomalies coincide with seasonal wet and dry variations.
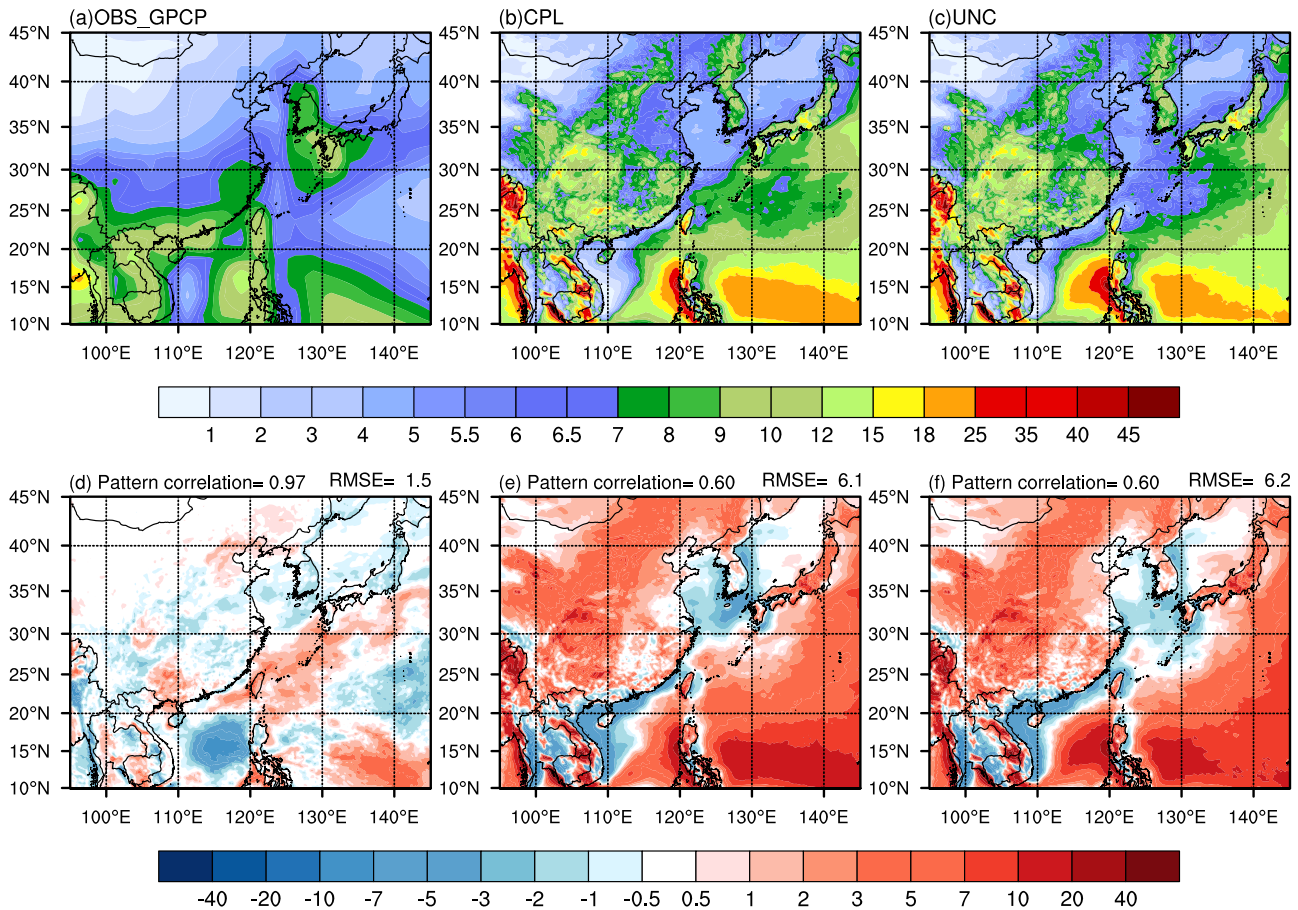
Fig. 2 Precipitation maps from observations and simulations. Spatial distributions of June–July–August (summer) climatology precipitation (mm day^{-1}) over the East Asia for the (**a**) observational Global Precipitation Climatology Project (GPCP), (**b**) simulation CPL and (**c**) simulation UNC during 1991–2014, and the differences between (**d**) CPL and UNC (CPL−UNC), (**e**) CPL and GPCP (CPL−GPCP), and (**f**) UNC and GPCP (UNC−GPCP).

Our analysis showed that, among the ocean regions, the center of reduction in JJA was located in the South China Sea under both present and future conditions (Fig. 3a, c). By contrast, the center of increase was seen in north South China Sea and the region of Pacific western boundary currents. The largest changes in winter precipitation resulting from sea–air coupling are mainly located over the Indochina Peninsula and southern China, while its influence over eastern China is relatively weaker compared to the summer season.

Atmosphere feedback to the ocean drives radiative anomalies

Atmosphere feedback to the ocean modifies the upward solar radiation (SWU) and the net solar surface radiative fluxes (SWN) under present day conditions (Supplementary Figs. 3–4). Relative to simulation UNC, the mean changes in the SWU and SWN in JJA for the whole domain were $+0.82 \pm 0.32$ and -1.49 ± 1.70 W m^{-2}, respectively, in simulation CPL during the time period 1991–2014 (Fig. 4, Supplementary Figs. 3–4). Over land, the mean SWU and SWN in JJA changed by 1.46 ± 0.67 and -2.91 ± 2.18 W m^{-2}, respectively, after sea–air coupling. Over the ocean, the mean SWU in JJA changed by 0.20 ± 0.18 W m^{-2} and the SWN at the surface changed by -0.11 ± 2.12 W m^{-2}.

Under present day conditions, the radiative forcing anomalies in JJA were predominantly influenced by changes in the land surface net longwave radiation (LWN) (Fig. 4 and Supplementary Fig. 4). The overall LWN over the entire domain showed a positive anomaly of $+2.74$ W m^{-2}, primarily driven by the positive change in the land LWN ($+5.75$ W m^{-2}). However, this positive effect was

partially counteracted by the impact of cooling resulting from the change in the ocean LWN (-0.19 ± 0.77 W m^{-2}). The negative land longwave upward radiation (LWU) (-6.74 ± 2.86 W m^{-2}) contributed mainly to the opposite sign of the LWN. During DJF, the proportion of the land LWU contribution to the entire domain was less than in JJA. In JJA, the total radiative fluxes (the net surface solar flux plus the net surface longwave flux) at the surface averaged over land and over the ocean were estimated to be 2.84 ± 1.04 and -0.30 ± 1.75 W m^{-2}, respectively, and in DJF the total radiative fluxes were simulated as 1.11 ± 0.63 W m^{-2} over land and $-0.09 \pm$ W m^{-2} over the ocean.

Under future conditions, the impact of sea–air coupling on the long-term changes in the radiation components in East Asia was examined. The future JJA SWU anomalies showed a spatial pattern similar to the present day, with an increase over the whole domain from 2016 to 2039. The averaged anomalies were estimated to be 0.33 ± 0.54 W m^{-2} over land and -0.24 ± 0.16 W m^{-2} over the ocean (Fig. 4c). By contrast, the LWU anomalies showed a decrease after 2016, with changes of -1.93 ± 1.81 W m^{-2} over land and -2.17 ± 1.23 W m^{-2} over the ocean (Fig. 4f). It is important to note that both the SWU and LWU anomalies derived from simulations for the future period were weaker than those observed under present day conditions.

Ocean–atmosphere coupling modifies the net radiation

The annual net radiation anomalies (-0.61 ± 3.90 W m^{-2}) were primarily offset by the latent and sensible heat flux anomalies during JJA (Fig. 4h−i and Supplementary Fig. 4e−f). There was a
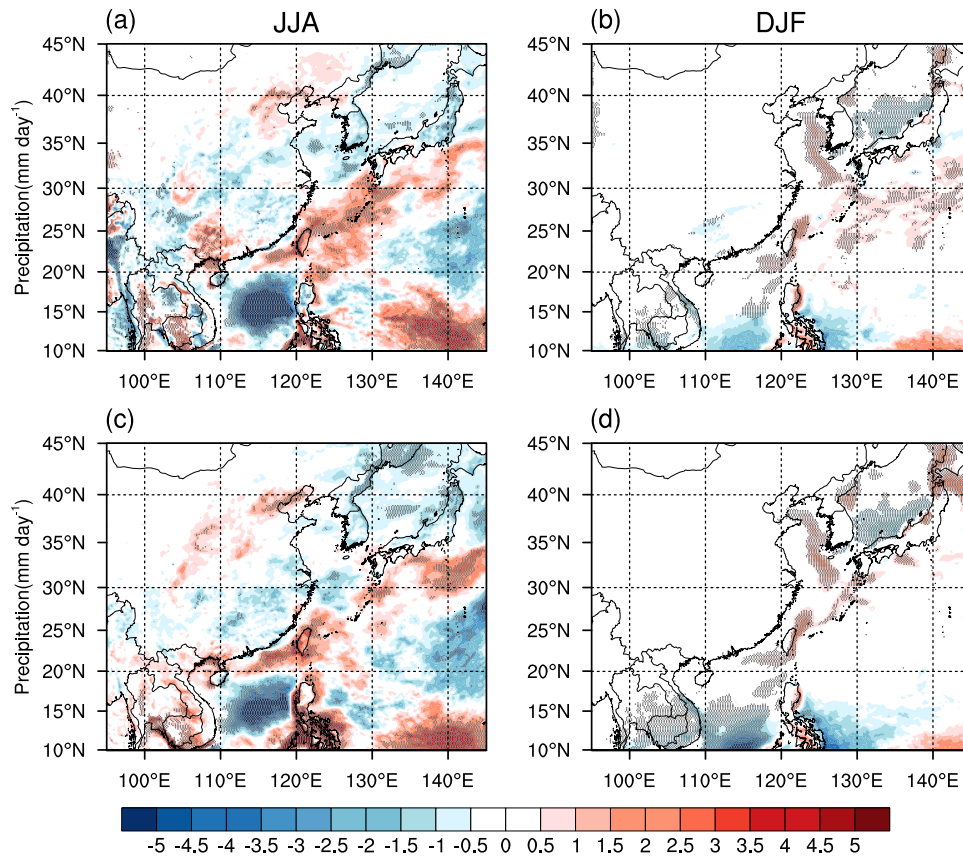
Fig. 3 Spatial distribution of the changes in precipitation attributed to sea–air coupling. The mean change in precipitation during (**a**, **c**) June–July–August and (**b**, **d**) December–January–February under (**a**, **b**) present day and (**c**, **d**) future conditions. The dotted areas indicate regions where the changes are statistically significant at the 95% confidence interval determined using Student's *t*-test.

substantial increase in the JJA latent heat flux ($3.69 \pm 3.64\,\mathrm{W\,m^{-2}}$) throughout the entire domain, which can be attributed to consistent anomalies over both the land ($6.91 \pm 3.31\,\mathrm{W^{-2}}$) and ocean ($0.57 \pm 5.84\,\mathrm{W^{-2}}$). As a consequence, the average JJA latent heat anomalies showed a noticeable increase from Northeast China (43–54° N and 110–135° E) to the South-Central Peninsula. An increase in the latent heat fluxes was seen in the offshore region of eastern China (15–35° N).

Under present day conditions, the changes in the sensible heat fluxes in JJA had an important role in regulating the net radiation anomalies (Fig. 4h). These changes were primarily manifested as negative sensible heat fluxes for whole domain ($-1.84 \pm 1.00\,\mathrm{W\,m^{-2}}$), which were determined by a decrease in the land-based fluxes ($-4.46 \pm 2.15\,\mathrm{W\,m^{-2}}$) during JJA, partially offset by an increase in the oceanic fluxes ($+0.71 \pm 0.47\,\mathrm{W\,m^{-2}}$). By contrast, both the land ($+0.44 \pm 0.44\,\mathrm{W\,m^{-2}}$) and ocean ($+1.30 \pm 0.82\,\mathrm{W\,m^{-2}}$) showed positive sensible heat fluxes during DJF, contributing to flux anomalies of the opposite sign. The sign of the sensible heat flux anomalies remained consistent in both JJA and DJF over land under future conditions. However, these anomalies were projected to be lower than those simulated under present day conditions.

Ocean–atmosphere coupling regulates the thermal asymmetry between the ocean and land

The land regions showed stronger cooling than the ocean. The annual mean T2 changed by -1.02 ± 1.17°C over land and by -0.23 ± 0.38°C in the ocean (Fig. 5 and Supplementary Table 1). These findings indicate an asymmetry in the changes in T2 between the ocean and land after sea–air coupling.

Spatially, the influence of ocean coupling under present day conditions resulted in significant cooling, primarily observed in the northern and eastern regions of China between the lower reaches of the Yellow River and the lower reaches of the Yangtze River (Fig. 5a). A remarkable cooling trend >3 °C was identified between 30 and 35° N during JJA. However, the intensity of the cooling effect decreased substantially in the areas located south of 30° N. In DJF, the temperature anomalies were lower, but there was a distinct cooling center with negative temperature anomalies in the eastern South-Central Peninsula.

The average temperature anomalies were relatively modest under future conditions, showing cooling predominantly over land (Fig. 5c). In particular, the most significant cooling due to sea–air coupling in JJA was observed north of 30° N. The area with the highest impact was located between the Korean Peninsula and the Japanese islands, where the cooling effect attributed to sea–air coupling was the strongest (less than -0.3 °C) for both present and future conditions. However, the impact of sea–air coupling under future conditions was noticeably weaker than that under present day conditions. The influence of sea–air coupling was weaker during DJF than during JJA.

Sea–air coupling has induced latitudinal asymmetric changes in land–sea near-surface temperatures. During the historical period, south of 30°N latitude, land cooling in summer was higher than over the ocean (Fig. 6), leading to a reduction of the land-sea temperature contrast by 0.6 ± 0.3 °C (s6). In the future period, the cooling of the land in summer remains slightly higher than over the ocean, leading to a reduction of the land-sea temperature contrast by 0.1 ± 0.2 °C. In winter, the land-sea temperature contrast decreased by 0.5 ± 0.2 °C in the historical period, while
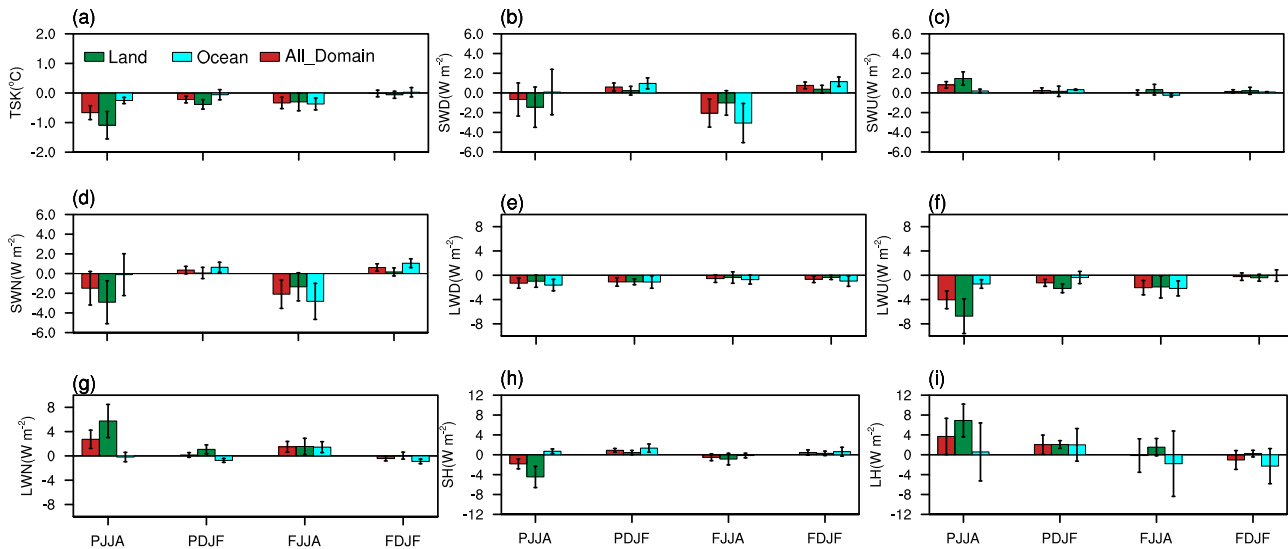
Fig. 4   Mean change over land, ocean and the whole domain. Mean change in (**a**) surface temperature, (**b**) downward solar radiation (SWD), (**c**) upward solar radiation (SWU), (**d**) net solar radiation (SWN), (**e**) downward longwave radiation (LWD), (**f**) upward longwave radiation (LWU), (**g**) net longwave radiation (LWN), (**h**) sensible heat fluxes (SH) and (**i**) latent heat fluxes (LH) following sea–air coupling in East Asia. The data are presented for both present day conditions during June–July–August (JJA) and December–January–February (DJF) and future conditions during June–July–August (JJA) and December–January–February (DJF). 'P' means the present conditions, and 'F' means the future conditions. The black error bar represents ±1 standard deviation.
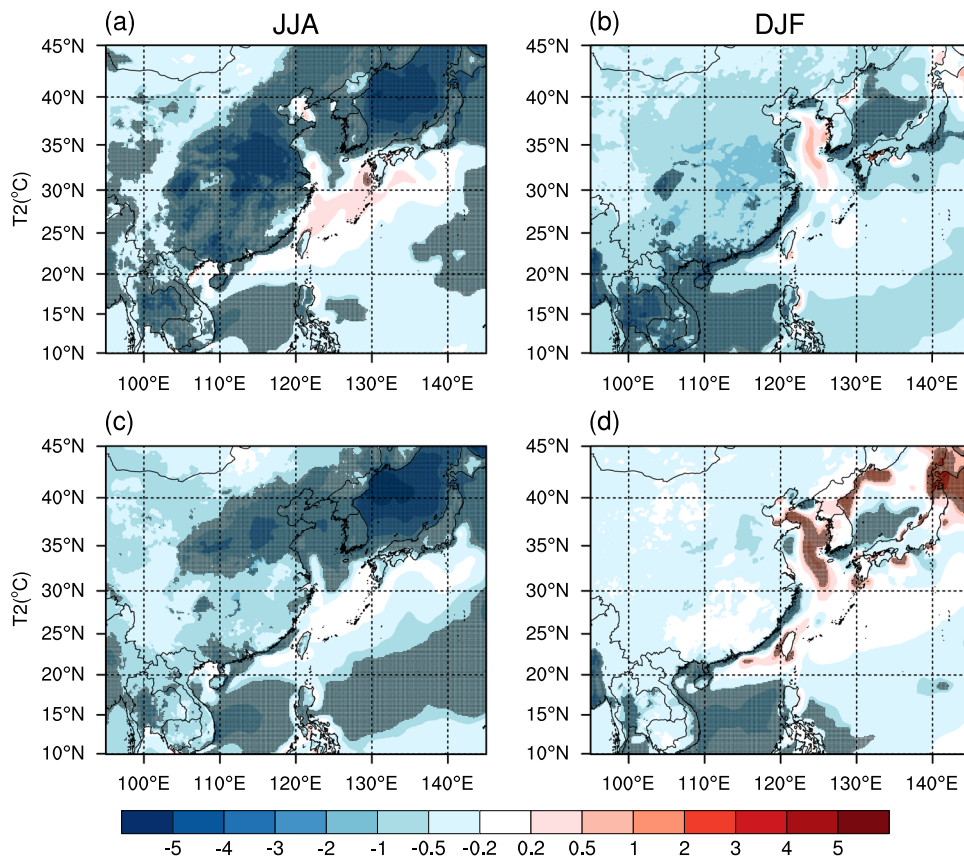

Fig. 5   Spatial distribution of the changes in the 2-m temperature (T2) attributed to sea–air coupling. The mean change in T2 during (**a**, **c**) June–July–August and (**b**, **d**) December–January–February under (**a**, **b**) present day and (**c**, **d**) future conditions. The dotted areas indicate regions where the changes are statistically significant at the 95% confidence interval determined using Student's *t*-test.
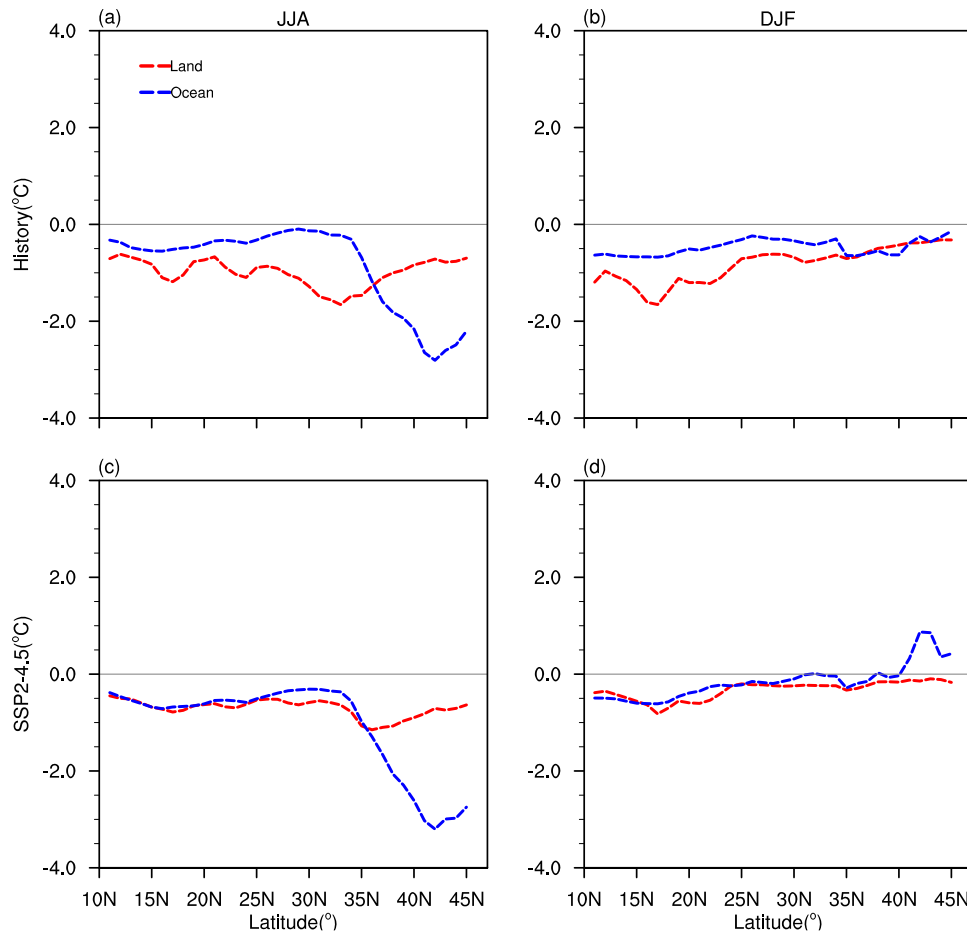
Fig. 6 Changes in the latitude–dependent 2-m temperature (T2) attributed to sea–air coupling. The mean change over land (red) and ocean (blue) in T2 during (**a**, **c**) June–July–August and (**b**, **d**) December–January–February under (**a**, **b**) present day and (**c**, **d**) future conditions.

the land-sea temperature contrast increases slightly by 0.01 ± 0.2 °C in the future period.

DISCUSSION

Sea–air coupling primarily influences water circulation processes in a region by altering the surface temperature and energy dynamics of the ocean[4,24,25]. However, quantitative assessments of the specific impacts of sea–air coupling have been limited[25]. We conducted simulations to investigate the changes in precipitation and circulation patterns across East Asia. Sea−air coupling in some regions of eastern and southern China resulted in a decrease in average precipitation during JJA by approximately 1.0 mm/day. This reduction accounts for approximately 13% of the total summer rainfall in these specific areas. A decrease in the land–sea land thermal contrast of 0.6 ± 0.3 °C were seen. There is also a decrease in latent heat in the southeast ocean within the domain, which is the source of moisture transport from the northwest Pacific to East Asia[33]. During JJA, fluctuations in the land–sea temperature contrast dynamically influence monsoon systems and then precipitation in East Asia. In addition, changes in the sea surface latent heat flux are a broad reflection of changes in sea surface evaporation. These shifts can affect the amount of moisture transported from the ocean to the land.

Recent studies have shown that ocean–atmosphere coupling has the potential to change the atmospheric heat contrast between land and ocean[34,35]. Such changes in the heat contrast can induce shifts in circulation patterns and affect precipitation patterns over land. This phenomenon may be related to the

land–ocean temperature contrast (Figs. 5 and S6), where warmer land relative to the ocean can stimulate enhanced atmospheric convergence over land, potentially resulting in additional precipitation[34]. However, variations in the heat contrast driven by ocean-atmosphere coupling in the East Asia and Northwest Pacific regions remain relatively unexplored. Therefore, one of the main objectives is to assess whether ocean-atmosphere coupling in East Asia has indeed altered the land-sea heat contrast and, if so, to investigate the relationship between this change and land precipitation in East Asia. This study uses a regional climate model to investigate how ocean–atmosphere interactions control these processes.

Sea–air coupling has a crucial role in modulating the latent heat fluxes of the southeast ocean within the domain located in the WNP. Southern winds carry warm, moisture-laden air from the WNP[3,25], facilitating the transportation of water toward East Asia. As a result, variations in precipitation across East Asia are closely linked to the prevailing supply of water vapor over the WNP[36]. Upward latent heat fluxes result in the release of latent heat of evaporation over the ocean surface[37,38]. Sea–air coupling led to a change in the latent heat fluxes of −3.76 ± 8.56 W m^{-2} (−0.13 ± 0.30 mm day^{-1} evaporation) in the WNP, excluding offshore eastern China, during the time period 1991–2014 (Supplementary Fig. 7). The main sources of moisture are from the northwest Pacific to East Asia, with a moisture contribution rate of 30%, highlighting the role of evaporation in the northwest Pacific for precipitation in East Asia[13,33]. Reduced evaporation in the northwest Pacific will reduce the amount of oceanic water vapor
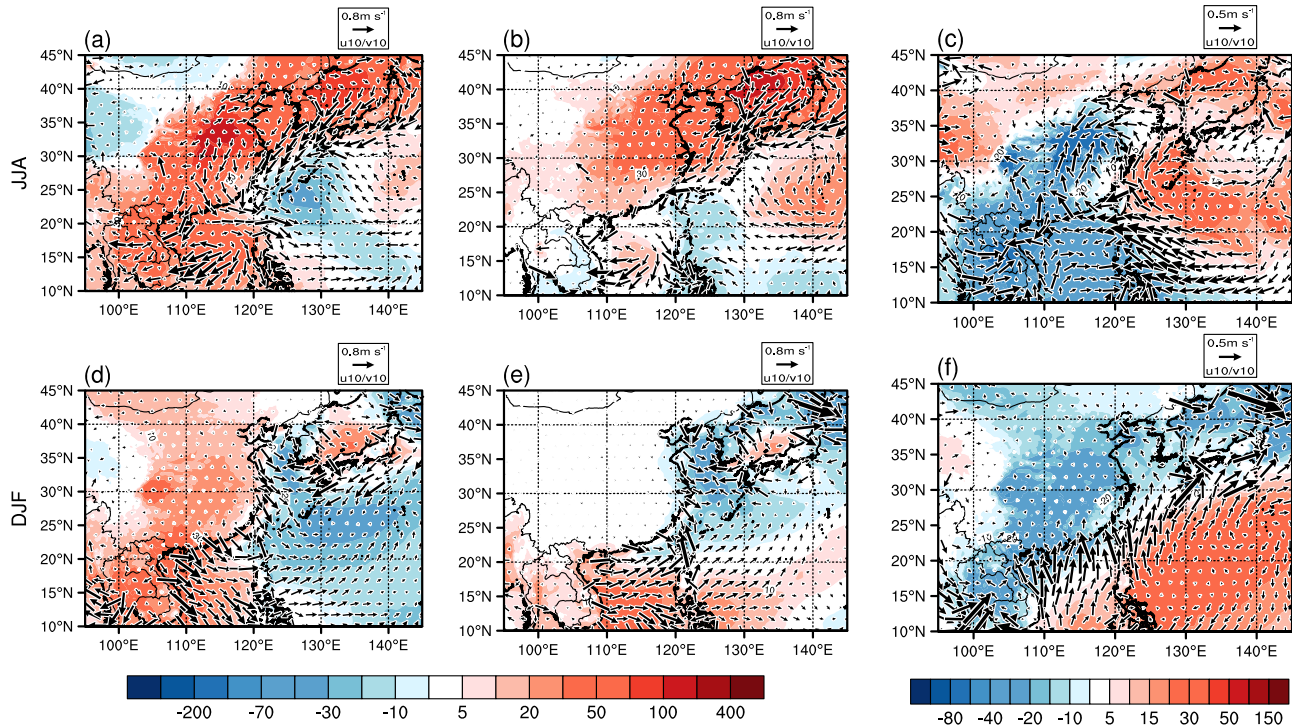
Fig. 7 Mean difference between simulations. Spatial distributions of the differences between simulations UNC and CPL for the mean surface pressure (Pa) (color scale) and U10/V10 (m s^{-1}) (vectors) during (**a**–**c**) June–July–August and (**d**–**f**) December–January–February under (**a**, **d**) present day conditions from 1991 to 2014, (**b**, **e**) future conditions during the time period 2016–2039. **c**, **f** Changes in the differences from future to present day conditions.

transported to East Asia, leading to reduced precipitation in East Asia[39,40].

Sea–air coupling weakened the thermal contrast between the land and sea, resulting in reduced precipitation in East Asia in JJA. During the JJA, the land cooled more than the ocean due to sea-air coupling. As a result, the temperature difference between land and ocean decreased. The changes in temperature asymmetry following sea–air coupling weakened the land–sea thermal contrast and reduced the latitudinal pressure gradient (Fig. 7). The reduced latitudinal pressure gradient attenuated the sea breeze from the eastern Pacific to the East Asian land area[41–43]. As a consequence, there was a decrease in the low-level East Asian monsoon flow (Fig. 7a), which contributed to a reduction in the Asian summer monsoon. In the future, ocean coupling is expected to cause a continued decrease in the sea–land pressure gradient (Fig. 7b). However, it is anticipated that changes in the strength of this gradient will be weaker than at the present day.

The southeast circulation from the northwest Pacific brings abundant water vapor into the South China Sea, which then affects eastern China via southern flows[25]. However, as shown in Fig. 7, during the historical period, resulting from sea–air coupling, an anomalous anticyclone was located over the northwest Pacific, centered at about 20°N and 128°E. Anomalous north flows prevailed in the northeastern, northern, eastern and southern regions of China, which hindered the transport of water vapor from the northwest Pacific to eastern China. As a result, there was a decrease in precipitation in East Asia during the historical period. In contrast, in the future period, the anomalous anticyclone over the northwest Pacific weakens and the anomalous northern flows decrease. This reduces the hindrance to water vapor transport from the northwest Pacific to East Asia. Therefore, the intensity of precipitation reduction in East Asia is expected to decrease in the future compared to the historical period.

The simulated stronger cooling over land can be primarily attributed to changes in the latent heat fluxes and SWU (Figs. S4 and S7). According to the Stefan–Boltzman law, the greater increase in the SWU over land than over the ocean could lead to stronger cooling (Supplementary Fig. 4). The increase in latent heat fluxes or intensified evapotranspiration over land (Supplementary Table 1), which requires energy, exerts a cooling influence[44,45]. These anomalies in surface radiation amplify the negative feedback of sea–air coupling on land temperatures during JJA, although its influence is diminished during DJF. Changes in land SWU and latent heat fluxes will continue to play an important role in influencing land surface temperatures during JJA under future conditions (Fig. 5).

When comparing the simulation after sea–air coupling with the control simulation, we observed an impact on the cloud fraction, particularly during JJA. The coupling between the sea and the atmosphere led to an increase in cloud cover (Supplementary Fig. 4), resulting in a reduction in the amount of solar radiation reaching the land surface (Fig. 5c). This change in the cloud fraction induced by sea–air coupling subsequently caused a decrease in the LWU from the surface (Fig. 4j). Oceanic clouds tend to contain higher levels of water vapor than those over land, making them potent GHGs that effectively absorb and re-emit the longwave radiation emitted by the Earth's surface back into the atmosphere. This process contributes to additional warming of the oceans. As a consequence, the cooling effect over the ocean is less pronounced than that over land (Fig. 5a).

Usually, internal climate variations lead to pronounced fluctuations in precipitation, covering a range from interannual to decadal time scales. In fact, precipitation variability exceeds mean precipitation. Global coupled models have also shown that precipitation variability exceeds its mean[46,47]. Sun and Ding[48] found that only about 15% of models can accurately capture decadal variations in precipitation. Presently, climate models

continue to face challenges in simulating variations in East Asian precipitation[49,50]. Uncertainty arising from atmospheric-ocean coupling is one of the inevitable primary sources[51]. The influence of ocean-atmosphere coupling on the variability of precipitation (Supplementary Fig. 3) suggests that uncertainties remain in the simulation of precipitation variability by regional models. It needs a further investigation in the future.

Our study has certain limitations in capturing the actual impact of ocean–atmosphere coupling on East Asia. Over the past few decades, there has been an increase in GHG emissions, which has resulted in the overwhelming majority (>90%) of the excess energy in the climate system being absorbed by the world's oceans[52]. This trend underscores the need for a more realistic consideration of this increase and its implications. The increase in GHG emissions has contributed to a heightened thermal contrast between the land surface and the oceans[53], resulting in increased monsoon rainfall in Asia[54]. Although the absence of explicit GHG dynamics may affect the intensity of temperature and precipitation in East Asia[12,55–57], it is important to note that our focus is specifically on ocean–atmosphere coupling under natural conditions. The impact of GHG emissions is a separate topic which will be considered in future research.

Certain Earth system models struggle to accurately reproduce the magnitude and intensity of the East Asian monsoon system[58,59]. However, it is well known that high-resolution RCM simulations of the monsoon system can improve the agreement with observations[60,61], thereby enhancing the accuracy of simulation results in the Asian monsoon region. The RCM indicates that ocean–atmosphere coupling modifies the monsoon intensity and precipitation by asymmetrically altering the thermal contrast between the ocean and land. The apparent decrease in monsoon precipitation in East Asia in JJA underscores the need to consider the role of sea–air coupling in this region because it has the potential to improve the accuracy of RCM projections and predictions.

Our analysis has shown that ocean coupling exerts an indirect influence on both the latent heat fluxes in the southeastern ocean and the atmospheric circulation in East Asia. This hinders the inflow of moisture from the WNP, which has a vital role in shaping the patterns of precipitation across East Asia. The estimated change in the latent heat fluxes in the southeastern ocean is about $-3.76 \pm 8.56\,\mathrm{W\,m^{-2}}$. The gradual decrease in the thermal contrast between the land and ocean, attributed to sea–air coupling during JJA, weakens the near-surface pressure gradient between the sea and land (Fig. 8). This weakening, in turn, adversely impacts the transport of water vapor from the ocean to the land surface. It is important to note that the intensity of this slowdown in the land–sea thermal contrast is projected to decrease in the future. The sea-air coupling, especially concentrated in northern and eastern China, is a major contributor to the decrease in precipitation in East Asia.

METHODS

Regional ocean–atmosphere coupled model

We used the Advanced Research Weather Research and Forecasting (ARW) Version 4.0 modeling system[62]. The WRF model has been widely applied in atmospheric research across various spatial and temporal scales[63–65] and was used here as an independent regional atmospheric model. The parameterization schemes for major atmospheric processes included the Rapid Radiative Transfer Model for General Circulation Models (RRTMG) shortwave and longwave radiation schemes[66], the Yonsei University Scheme for the Planetary Boundary Layer (YSU PBL)[67], the Purdue Lin Scheme for microphysics parameterization[68], the Kain–Fritsch cumulus convective parameterization scheme[69] and the Noah land surface model with multi-parameterization options (Noah-
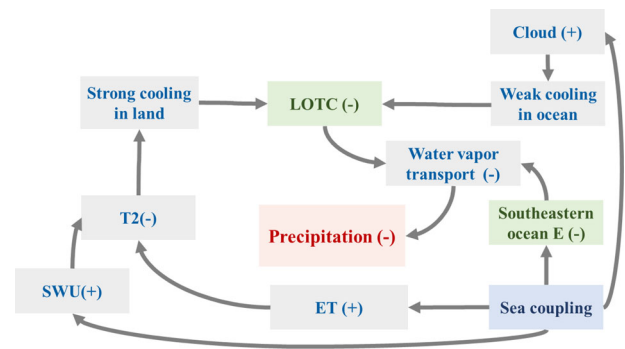

Fig. 8 Schematic diagram showing the changes in precipitation over East Asia following sea–air coupling. The diagram highlights the impact of sea-coupled processes on factors including ocean evaporation (E), cloud fraction, the 2-m temperature (T2), land evaporation (ET), land–sea thermal asymmetry (LOTC), upward solar radiation (SWU) and water vapor transport. These changes collectively contribute to a decrease in summer (June–July–August) precipitation over East Asia. The changes in the asymmetries of the sea–land thermal contrasts and the ocean evaporation have important roles in driving these changes. In the diagram, the symbols '+' and '−' represent increases or decreases in the respective variables, respectively.

Table 1. The model used in this study and its characteristics.

Atmospheric model configuration and physical schemes	
Horizontal resolution	15 km
Horizontal grids	346 × 311
Vertical layers	35
Radiation Physics	RRTMG[66]
Microphysics	Lin[68]
Cumulus Physics	Kain–Fritsch[69]
PBL Physics	YSU[67]
Land Surface Model	Noah-MP[70,71]
Vegetation Physical Progress	Dynamic
Canopy Stomatal Resistance	Ball-Berry[72]
Soil Moisture Factor for Stomatal Resistance	Noah scheme
Runoff and Groundwater	SIMGM[73]
Surface Layer Drag Coefficient	Monin-Obukhov
Supercooled Liquid Water	NY06[74]
Frozen Soil Permeability	Koren99[75]
Radiation Transfer	Two-stream applied to vegetated fraction[76]
Snow Surface Albedo	CLASS[77]
Rainfall and Snowfall	Jordan91[78]

MP[70,71] for land surface processes. Table 1 gives further details of the parameterization options for the land surface processes.

The WRF model did not include an ocean component. However, for the purposes of this study, the ocean component was coupled into the WRF model using LICOM. This coupled regional ocean–atmosphere model system (WRF-LICOM) consists of regional atmosphere and ocean components. LICOM is a regional version of the quasi-global eddy ocean general circulation model, which is based on LICOM Version 2.0 and is also known as the North Pacific model (LICOM_np)[72]. LICOM_np covers the region (10° S–66.0° N, 98° E–74.9° W) with a horizontal resolution of 0.1° and 55 vertical layers. The coupling between the atmospheric and oceanic models was achieved through the Ocean Atmosphere Sea

Ice Soil Coupler Version 3 (OASIS3)[73] at 60-min intervals. This coupling enabled the atmospheric model to receive updated SSTs, sea ice thickness and surface currents from the ocean component through a grid area-weighted interpolation scheme, while the surface wind stresses, water and heat fluxes from the atmosphere were interpolated to the ocean in a similar manner[74,75].

The regional atmospheric and ocean model was both forced with data from a bias-corrected global dataset. This dataset was constructed using 18 models from the Coupled Model Intercomparison Project Phase 6 (CMIP6) and has been bias-corrected using the European Centre for Medium-Range Weather Forecasts Reanalysis 5 (ERA5) dataset[76]. The bias-corrected dataset has a reanalysis bias climatological mean and interannual variance, but with a long-term trend from ensemble mean of 18 CMIP6 models. The dataset has a horizontal grid spacing of 1.25° and covers the historical period 1979–2014 and the future period 2015–2100 at 6-h intervals.

For the future period, the shared socioeconomic pathway (SSP) 2–4.5 scenario was used, which represents an intermediate greenhouse gas (GHG) emission scenario with CO_2 emissions around current levels until 2050, followed by a gradual decline without reaching net zero by 2100[77]. The initial conditions for the atmospheric model were provided by the combined and bias-corrected dataset whereas the initial conditions for the ocean model were obtained from an offline multi-year LICOM run that was also forced with a bias-corrected global dataset. The bias-corrected dataset were generated using an empirical quintile mapping method[78–85]. Here, we also employed an ensemble mean long-term trend derived from CMIP6 models similar to the bias-corrected data used to drive atmospheric model.

Simulations
An uncoupled simulation of the RCM forced by prescribed SSTs was performed as a control run (UNC). In addition, a simulation was conducted using the coupled model of the RCM (CPL) to investigate the effects of ocean–atmosphere coupling. These two long-term regional simulations were conducted using the same bias-corrected global datasets. Simulation UNC included an individual atmospheric component, whereas simulation CPL consisted of both atmospheric and ocean coupling components. For both UNC and CPL simulations, we used the MODIS-based land use classification dataset with 30-second resolution and 21 categories, horizontally interpolated to 15-km resolution grids.

It is important to note that the GHG concentrations in the two simulations remained constant (e.g., the volume-mixing ratio for CO_2 was 379.0 ppm). This means that the external forcing from GHGs was only represented in the lateral boundary fields of the atmospheric model.

The simulations were conducted to investigate the present day conditions from 1990 to 2014 and the future conditions under the SSP2–4.5 scenario from 2016 to 2039. For our future projections, we have used a bias-corrected global dataset derived from GCM models within the CMIP6 framework. The CMIP6 projections begin in 2015. The first year, 2015, was referred to as the spin-up period, followed by an analysis of the subsequent 24-year simulations covering the near future period from 2016 to 2039. This period corresponds to the 24-year historical simulations from 1991 to 2014.

The atmospheric components in the two simulations were configured with a horizontal resolution of 15 km and 35 vertical layers, with the model top at 50 hPa. The individual atmosphere domain of simulation UNC and the ocean–atmosphere interactive domain of simulation CPL were centered at (32° N, 120° E) and covered East Asia and the adjacent oceans with a grid size of (346 × 311). The ocean component of simulation CPL covered the entire Pacific Ocean in the northern hemisphere with a horizontal resolution 1/10° and a vertical resolution 55 layers, respectively (Fig. 1). It was also forced by the bias-corrected global dataset, but with different forcing fields.

A pair of 24-year simulations were run, one for historical periods and one for future periods, each with a different spin-up period. The spin-up years were chosen to be 1990 for the historical simulation and 2015 for the future simulation. Consequently, simulations were performed for the historical period from 1991 to 2014 and for the future period from 2016 to 2039. The ocean component from the simulation CPL was initialized using offline LICOM_np final outputs at 00:00 UTC on January 1, 1990, and this offline LICOM_np simulation is conducted from 00:00 UTC on January 1, 1985 to 00:00 UTC on January 1, 1990. The atmospheric component in simulation UNC obtained the SST from the forcing field, which was updated every 6 h, whereas the atmosphere component in simulation CPL updated the SST from the ocean model LICOM every hour.

The model configurations and lateral boundary fields for the atmospheric component of simulations UNC and CPL were the same, with the only difference being the simulations with and without ocean–atmosphere interactions, respectively. The influence of regional ocean–atmosphere interactions were derived from simulations UNC and CPL.

Used methods
Precipitation patterns are influenced by the interplay of the ocean–land thermal contrast (LOTC) and energy transport[86]. To investigate the impact of sea–air coupling, we examined the changes in the LOTC before and after its implementation. The LOTC is determined by calculating the difference in 2-m air temperature (T2) between the land (0°–30°N) and ocean (0°–30°N) within the study domain using the formula:

$$LOTC = T2_{land}^{0-30°N} - T2_{ocean}^{0-30°N} \qquad (1)$$

where $T2_{land}^{0-30°N}$ is the area-weighted mean T2 of the land between 0°–30°N and $T2_{ocean}^{0-30°N}$ is the area-weighted mean T2 of the ocean surface between 0°–30°N within the domain. The LOTC is positive during the June–July–August (JJA) because the land is warmer than the ocean. A negative change in the LOTC indicates a decrease in the thermal contrast between the land and ocean, whereas a positive change signifies an increase in the contrast.

REFERENCES
1. Ren, G. et al. Historical and recent change in extreme climate over east asia. *Clim. Change* **168**, 22 (2021).
2. Thackeray, C. W. et al. Constraining the increased frequency of global precipitation extremes under warming. *Nat. Clim. Change* **12**, 441–448 (2022).
3. Yihui, D. & Chan, J. C. L. The east asian summer monsoon: An overview. *Meteorol. Atmos. Phys.* **89**, 117–142 (2005).
4. Kim, E. -J. & Hong, S. -Y. Impact of air-sea interaction on east asian summer monsoon climate in wrf. *J. Geophys. Res. Atmosph.* **115**, D19118 (2010).
5. Korell, L. et al. Responses of plant diversity to precipitation change are strongest at local spatial scales and in drylands. *Nat. Commun.* **12**, 2489 (2021).

6. Zhang, W. et al. Constraining extreme precipitation projections using past precipitation variability. *Nat. Commun.* **13**, 6319 (2022).

7. Kajbaf, A. A., Bensi, M. & Brubaker, K. L. Temporal downscaling of precipitation from climate model projections using machine learning. *Stoch. Environ. Res. Risk Assess.* **36**, 2173–2194 (2022).

8. Rodríguez, J. M., Milton, S. F. & Marzin, C. The east asian atmospheric water cycle and monsoon circulation in the met office unified model. *J. Geophys. Res. Atmosph.* **122**, 10246–210265 (2017).

9. Kaboth-Bahr, S. et al. A tale of shifting relations: East asian summer and winter monsoon variability during the holocene. *Sci. Rep.* **11**, 6938 (2021).

10. Yu, T. et al. Roles of enso in the link of the east asian summer monsoon to the ensuing winter monsoon. *J. Geophys. Res.: Atmosph.* **126**, e2020JD033994 (2021).

11. Wang, B. & Ding, Q. Global monsoon: Dominant mode of annual variation in the tropics. *Dyn. Atmosph. Oceans* **44**, 165–183 (2008).

12. Liang, W. & Zhang, M. Summer and winter precipitation in east asia scale with global warming at different rates. *Commun. Earth Environ.* **2**, 150 (2021).

13. Cheng, T. F., Lu, M. & Dai, L. Moisture channels and pre-existing weather systems for east asian rain belts. npj Climate and Atmospheric. *Science* **4**, 32 (2021).

14. Chang, C.-P., Zhang, Y. & Li, T. Interannual and interdecadal variations of the east asian summer monsoon and tropical pacific ssts. Part ii: Meridional structure of the monsoon. *J. Clim.* **13**, 4326–4340 (2000).

15. Chen, G. & Huang, R. Interannual variations in mixed rossby–gravity waves and their impacts on tropical cyclogenesis over the western north pacific. *J. Clim.* **22**, 535–549 (2009).

16. Lu, R., Dong, B. & Ding, H. Impact of the atlantic multidecadal oscillation on the asian summer monsoon. *Geophys. Res. Lett.* **33**, L24701 (2006).

17. Chen, S. et al. Impacts of the atlantic multidecadal oscillation on the relationship of the spring arctic oscillation and the following east asian summer monsoon. *J. Clim.* **33**, 6651–6672 (2020).

18. Zheng, F. et al. Influence of the summer nao on the spring-nao-based predictability of the east asian summer monsoon. *J. Appl. Meteorol. Climatol.* **55**, 1459–1476 (2016).

19. Matsumura, S. & Horinouchi, T. Pacific ocean decadal forcing of long-term changes in the western pacific subtropical high. *Sci. Rep.* **6**, 37765 (2016).

20. Shi, J. et al. Possible modulation of the interannual enso-east asian winter monsoon relationship by the north american ice sheets during the last 21 ka. *Geophys. Res. Lett.* **47**, e2020GL089572 (2020).

21. Sang, Y.-F. et al. Does summer precipitation in china exhibit significant periodicities? *J. Hydrol.* **581**, 124289 (2020).

22. Qian, C. & Zhou, T. Multidecadal variability of north china aridity and its relationship to pdo during 1900–2010. *J. Clim.* **27**, 1210–1222 (2014).

23. Wang, M. et al. Precipitation in eastern china over the past millennium varied with large-scale climate patterns. *Commun. Earth Environ.* **3**, 321 (2022).

24. Giorgi, F. & Gao, X.-J. Regional earth system modeling: Review and future directions. *Atmos. Ocean. Sci. Lett.* **11**, 189–197 (2018).

25. Dai, Y., Li, H. & Sun, L. The simulation of east asian summer monsoon precipitation with a regional ocean-atmosphere coupled model. *J. Geophys. Res. Atmosph.* **123**, 11362–311376 (2018).

26. Shi, P. et al. Significant land contributions to interannual predictability of east asian summer monsoon rainfall. *Earth's Fut.* **9**, e2020EF001762 (2021).

27. Huang, Y. et al. On the air-sea couplings over tropical pacific: An instantaneous coupling index using dynamical systems metrics. *Geophys. Res. Lett.* **49**, e2021GL097049 (2022).

28. Zou, L. & Zhou, T. Can a regional ocean–atmosphere coupled model improve the simulation of the interannual variability of the western north pacific summer monsoon? *J. Clim.* **26**, 2353–2367 (2013).

29. Xue, P. et al. Coupled ocean-atmosphere modeling over the maritime continent: A review. *J. Geophys. Res. Oceans* **125**, e2019JC014978 (2020).

30. Cha, D.-H. et al. Improvement of regional climate simulation of east asian summer monsoon by coupled air–sea interaction and large-scale nudging. *Int. J. Climatol.* **36**, 334–345 (2016).

31. Wu, R. & Kirtman, B. Regimes of local air-sea interactions and implications for performance of forced simulations. *Clim. Dyn.* **29**, 393–410 (2007).

32. Zhou, T., Wu, B. & Wang, B. How well do atmospheric general circulation models capture the leading modes of the interannual variability of the asian–australian monsoon? *J. Clim.* **22**, 1159–1173 (2009).

33. Shi, Y. et al. A lagrangian analysis of water vapor sources and pathways for precipitation in east china in different stages of the east asian summer monsoon. *J. Clim.* **33**, 977–992 (2022).

34. Yeh, S.-W. et al. Contrasting response of hydrological cycle over land and ocean to a changing co2 pathway. *npj Clim. Atmos. Sci.* **4**, 53 (2021).

35. Richardson, T. B. et al. Drivers of precipitation change: An energetic understanding. *J. Clim.* **31**, 9641–9657 (2018).

36. Li, X. et al. Decadal transition of the leading mode of interannual moisture circulation over east asia–western north pacific: Bonding to different evolution of enso. *J. Clim.* **32**, 289–308 (2019).

37. Gao, S., Chiu, L. S. & Shie, C.-L. Trends and variations of ocean surface latent heat flux: Results from gsstf2c data set. *Geophys Res Lett.* **40**, 380–385 (2013).

38. Edwards, J. M. Oceanic latent heat fluxes: Consistency with the atmospheric hydrological and energy cycles and general circulation modeling. *J. Geophys. Res.: Atmosph.* **112**, D06115 (2007).

39. van der Ent, R. J. & Savenije, H. H. G. Oceanic sources of continental precipitation and the correlation with sea surface temperature. *Water Resour. Res.* **49**, 3993–4004 (2013).

40. Sun, B. & Wang, H. Analysis of the major atmospheric moisture sources affecting three sub-regions of east china. *Int. J. Climatol.* **35**, 2243–2257 (2015).

41. Wang, B., Wu, R. & Fu, X. Pacific–east asian teleconnection: How does enso affect east asian climate? *J. Clim.* **13**, 1517–1536 (2000).

42. Tanimoto, H. et al. Significant latitudinal gradient in the surface ozone spring maximum over east asia. *Geophys. Res. Lett.* **32**, L21805 (2005).

43. Wang, B. et al. Recent change of the global monsoon precipitation (1979–2008). *Clim. Dyn.* **39**, 1123–1135 (2012).

44. Jeong, S. -J. et al. Reduction of spring warming over east asia associated with vegetation feedback. *Geophys. Res. Lett.* **36**, L18705 (2009).

45. Shen, M. et al. Evaporative cooling over the tibetan plateau induced by vegetation growth. *Proc. Natl Acad. Sci.* **112**, 9299–9304 (2015).

46. Kim, Y.-H. et al. Evaluation of the cmip6 multi-model ensemble for climate extreme indices. *Weather Clim. Extr.* **29**, 100269 (2020).

47. Dong, T. & Dong, W. Evaluation of extreme precipitation over asia in cmip6 models. *Clim. Dyn.* **57**, 1751–1769 (2021).

48. Sun, Y. & Ding, Y. H. An assessment on the performance of ipcc ar4 climate models in simulating interdecadal variations of the east asian summer monsoon. *Acta Meteor. Sin.* **22**, 472–488 (2008).

49. Song, F. & Zhou, T. The climatology and interannual variability of east asian summer monsoon in cmip5 coupled models: Does air–sea coupling improve the simulations? *J. Clim.* **27**, 8761–8777 (2014).

50. Jiang, D. et al. Differences between cmip6 and cmip5 models in simulating climate over china and the east asian monsoon. *Adv. Atmos. Sci.* **37**, 1102–1118 (2020).

51. Wood, R. R. et al. Changes in precipitation variability across time scales in multiple global climate model large ensembles. *Environ. Res. Lett.* **16**, 084022 (2021).

52. Cai, W. et al. Southern ocean warming and its climatic impacts. *Sci. Bull.* **68**, 946–960 (2023).

53. Joshi, M. M., Lambert, F. H. & Webb, M. J. An explanation for the difference between twentieth and twenty-first century land–sea warming ratio in climate models. *Clim. Dyn.* **41**, 1853–1869 (2013).

54. Wang, B. et al. Global monsoon: Concept and dynamic response to anthropogenic warming. *Mausam* **74**, 493–502 (2023).

55. You, Q. et al. Recent frontiers of climate changes in east asia at global warming of 1.5 °C and 2 °C. *npj Clim. Atmos. Sci.* **5**, 80 (2022).

56. Peng, J. et al. Spatially varying in CO_2 concentrations regulates carbon uptake in the northern hemisphere. *J. Geophys. Res. Atmosph.* **n/a**, e2022JD037732 (2022).

57. Peng, J. et al. Overestimated terrestrial carbon uptake in the future owing to the lack of spatial variations co2 in an earth system model. *Earth's Future* **10**, e2021EF002440 (2022).

58. Tong, M., Zheng, Z. & Fu, Q. Evaluation of east asian meiyu from cmip6/amip simulations. *Clim. Dyn.* **59**, 2429–2444 (2022).

59. Jiang, W. et al. Biases and improvements of the enso-east asian winter monsoon teleconnection in cmip5 and cmip6 models. *Clim. Dyn.* **59**, 2467–2480 (2022).

60. Gao, X. et al. Reduction of future monsoon precipitation over china: Comparison between a high resolution rcm simulation and the driving gcm. *Meteorol. Atmos. Phys.* **100**, 73–86 (2008).

61. Mishra, A. K., Dubey, A. K. & Dinesh, A. S. Diagnosing whether the increasing horizontal resolution of regional climate model inevitably capable of adding value: Investigation for indian summer monsoon. *Clim. Dyn.* **60**, 1925–1945 (2023).

62. Skamarock, W. C. A description of the advanced research wrf version 3. *Ncar Tech.* **113**, 7–25 (2005).

63. Leung, L. R., Kuo, Y. H. & Tribbia, J. Research needs and directions of regional climate modeling using wrf and ccsm. *B Am. Meteorol. Soc.* **87**, 1747–1751, (2006).

64. Powers, J. G. et al. The weather research and forecasting (wrf) model: Overview, system efforts, and future directions. *B. Am. Meteorol. Soc.* **98**, 1717–1737 (2017).

65. Li, K. et al. The role of soil temperature feedbacks for summer air temperature variability under climate change over east asia. *Earth's Future* **10**, e2021EF002377 (2022).

66. Iacono, M. J. et al. Radiative forcing by long-lived greenhouse gases: Calculations with the aer radiative transfer models. *J. Geophys. Res.: Atmosph.* **113**, D13103 (2008).

67. Hong, S. Y., Noh, Y. & Dudhia, J. A new vertical diffusion package with an explicit treatment of entrainment processes. *Monthly Weather Rev.* **134**, 2318 (2006).

68. Chen, S.-H. & Sun, W.-Y. A one-dimensional time dependent cloud model. *J. Meteorolog. Soc. Jpn. Ser. II* **80**, 99–118 (2002).

69. Kain, J. S. The kain–fritsch convective parameterization: An update. *J. Appl. Meteorol.* **43**, 170–181 (2004).

70. Niu, G. Y. et al. The community noah land surface model with multi-parameterization options (noah-mp): 1. Model description and evaluation with local-scale measurements. *J. Geophys. Res. Atmos.* **116**, D12109 (2011).

71. Yang, Z. L. et al. The community noah land surface model with multi-parameterization options (noah-mp): 2. Evaluation over global river basins. *J. Geophys. Res.-Atmos.* **116**, D12110 (2011).

72. Yu, Y., Liu, H. & Lin, P. A quasi-global 1/10° eddy-resolving ocean general circulation model and its preliminary results. *Chin. Sci. Bull.* **57**, 3908–3916 (2012).

73. Valcke, S. Oasis3 user guide (prism_2-5) cerfacs technical support. OASIS3 User Guide (prism-2-5) CERFACS Technical Support, (2006).

74. Luo, J. J. et al. Reducing climatology bias in an ocean-atmosphere cgcm with improved coupling physics. *J. Clim.* **18**, 2344–2360 (2005).

75. Zou, L., Zhou, T. & Liu, H. Performance of a high resolution regional ocean–atmosphere coupled model over western north pacific region: Sensitivity to cumulus parameterizations. *Clim. Dyn.* **53**, 4611–4627 (2019).

76. Xu, Z. et al. Bias-corrected cmip6 global dataset for dynamical downscaling of the historical and future climate (1979–2100). *Sci. Data* **8**, 293 (2021).

77. O'Neill, B. C. et al. The scenario model intercomparison project (scenariomip) for cmip6. *Geosci. Model Dev.* **9**, 3461–3482 (2016).

78. Iturbide, M. et al. The r-based climate4r open framework for reproducible climate data access and post-processing. *Environ. Model Softw.* **111**, 42–54 (2019).

79. Ball, J. T., Woodrow, I. E. & Berry, J. A. A model predicting stomatal conductance and its contribution to the control of photosynthesis under different environmental conditions. In: Biggins J. *Progress in photosynthesis research: Volume 4 proceedings of the viith international congress on photosynthesis providence, rhode island*, USA, august 10–15, 1986. Dordrecht: Springer Netherlands. 1987. 221-224

80. Niu, G. -Y. et al. Development of a simple groundwater model for use in climate models and evaluation with gravity recovery and climate experiment data. *J. Geophys. Res.: Atmosph.* 112, (2007).

81. Niu, G. Y. & Yang, Z. L. Effects of frozen soil on snowmelt runoff and soil water storage at a continental scale. *J. Hydrometeorol.* **7**, 937–952 (2006).

82. Koren, V. et al. A parameterization of snowpack and frozen ground intended for ncep weather and climate models. *J. Geophys. Res.-Atmos.* **104**, 19569–19585 (1999).

83. Niu G. Y., Yang Z. L. Effects of vegetation canopy processes on snow surface energy and mass balances. *J. Geophys. Res.-Atmos.* 109, (2004).

84. Verseghy, D. L. Class-a canadian land surface scheme for gcms .1. Soil model. *Int. J. Climatol.* **11**, 111–133 (1991).

85. Jordan R. E. A one-dimensional temperature model for a snow cover : Technical documentation for sntherm.89. In: Proceedings of the 1991.

86. Yao, Y. et al. Rapid changes in land-sea thermal contrast across china's coastal zone in a warming climate. *J. Geophys. Res. Atmosph.* **124**, 2049–2067 (2019).

AUTHOR CONTRIBUTIONS

J.P. designed this study and wrote the manuscript. K.L. performed the simulations and data analyses. Both J.P. and K.L. contributed equally to this work. L.D., X.T., Z.X., L.Z., H.Z., and T.Z. contributed to the analysis of the results. All authors made significant contributions to the discussion of content and interpretation of findings.

COMPETING INTERESTS

The authors declare no competing interests.

ADDITIONAL INFORMATION

Supplementary information The online version contains supplementary material available at https://doi.org/10.1038/s41612-023-00498-w.

Correspondence and requests for materials should be addressed to Jing Peng or Kai Li.

Reprints and permission information is available at http://www.nature.com/reprints

Publisher's note Springer Nature remains neutral with regard to jurisdictional claims in published maps and institutional affiliations.